Climate Dynamics (2023) 61:4773–4791
https://doi.org/10.1007/s00382-023-06832-5

The onset and cessation of rainy season over the Hengduan Mountains

Weichen Tao[1] · Gang Huang[1,2,3] · Pengfei Wang[1,4] · Ya Wang[1] · Hainan Gong[4] · Danhong Dong[5]

Received: 19 August 2022 / Accepted: 16 May 2023 / Published online: 23 May 2023

Abstract

In this study, the onset and cessation of rainy season over the Hengduan Mountains (HM) are determined by an objective method. The onset and cessation of climatological rainy season are largely controlled by large-scale circulation systems, such as the Indian summer monsoon (ISM), 200 hPa subtropical jet, and the South Asian high. Both onset and cessation dates exhibit strong interannual variability. For late onset, the lower-level northeasterly anomalies over the north Indian Ocean (IO) delay the advance of moisture transported by ISM, and are excited by the positive SST anomalies over the southwest IO. In accord with late cessation, the equatorial west IO cooling adjusts the zonal overturn circulation and causes the west side wet anomalies, which trigger the north IO cyclonic wind anomalies and the northwest Pacific anticyclonic wind anomalies following Gill response. These two anomalous flows merge, turn southerly, and continuously transport moisture to the HM, prolonging the rainy season. At upper levels, the late onset and cessation related circulation anomalies are almost mirror images and highly resemble the Silk Road pattern. The anomalous upper and lower-level circulation cooperate and favor the dynamical and thermodynamical processes, which contribute to the vertical motion anomalies and finally affect the onset and cessation dates. Especially, the 200 hPa geopotential height anomaly center on the north side of the Arabian Sea (AS) is stronger than the other centers both for late onset and cessation, and coincides well with the nearby Rossby wave source, which are reinforced via the planetary vorticity stretching term due to the upper-level wind anomalies induced by the IO SST anomalies.

Keywords Onset and cessation date · Rainy season · Hengduan Mountains · Omega equation · Silk Road pattern · Rossby wave source

1 Introduction

The Hengduan Mountains (HM) lie on Southwest China and the southeast side of the Tibetan Plateau (TP), with latitude and longitude ranging from 24° N to 35° N and 96° E to 105° E, respectively (Fig. 1a). The word "Hengduan" means "block" in Chinese, and this region gets its name because that the HM has a unique three-dimensional landscape featured with high mountains and deep valleys and blocks east–west traffic. The HM shows the world's steepest elevation drop, ranging from the TP at about 4800 m to the Sichuan basin at about 600 m in the distance of 500 km. Several major Asian rivers, as the Yangtze River and the Yellow River in China, the Mekong River and the Salween River over the Indochina Peninsula, and so on, originate from or flow through this region. Besides, the HM is a global biodiversity hotspot and have more than 12,000 species of vascular flora (e.g., Myers et al. 2000; Nie et al. 2002; Xing and Ree 2017; Cheng et al. 2018), flourishing in a diverse

✉ Gang Huang
hg@mail.iap.ac.cn

1 State Key Laboratory of Numerical Modeling for Atmospheric Sciences and Geophysical Fluid Dynamics, Institute of Atmospheric Physics, Chinese Academy of Sciences, Beijing 100029, China

2 Laboratory for Regional Oceanography and Numerical Modeling, Qingdao National Laboratory for Marine Science and Technology, Qingdao 266237, China

3 University of Chinese Academy of Sciences, Beijing 100049, China

4 Center for Monsoon System Research, Institute of Atmospheric Physics, Chinese Academy of Sciences, Beijing 100029, China

5 Bureau of Major R&D Programs, Chinese Academy of Sciences, Beijing 100864, China

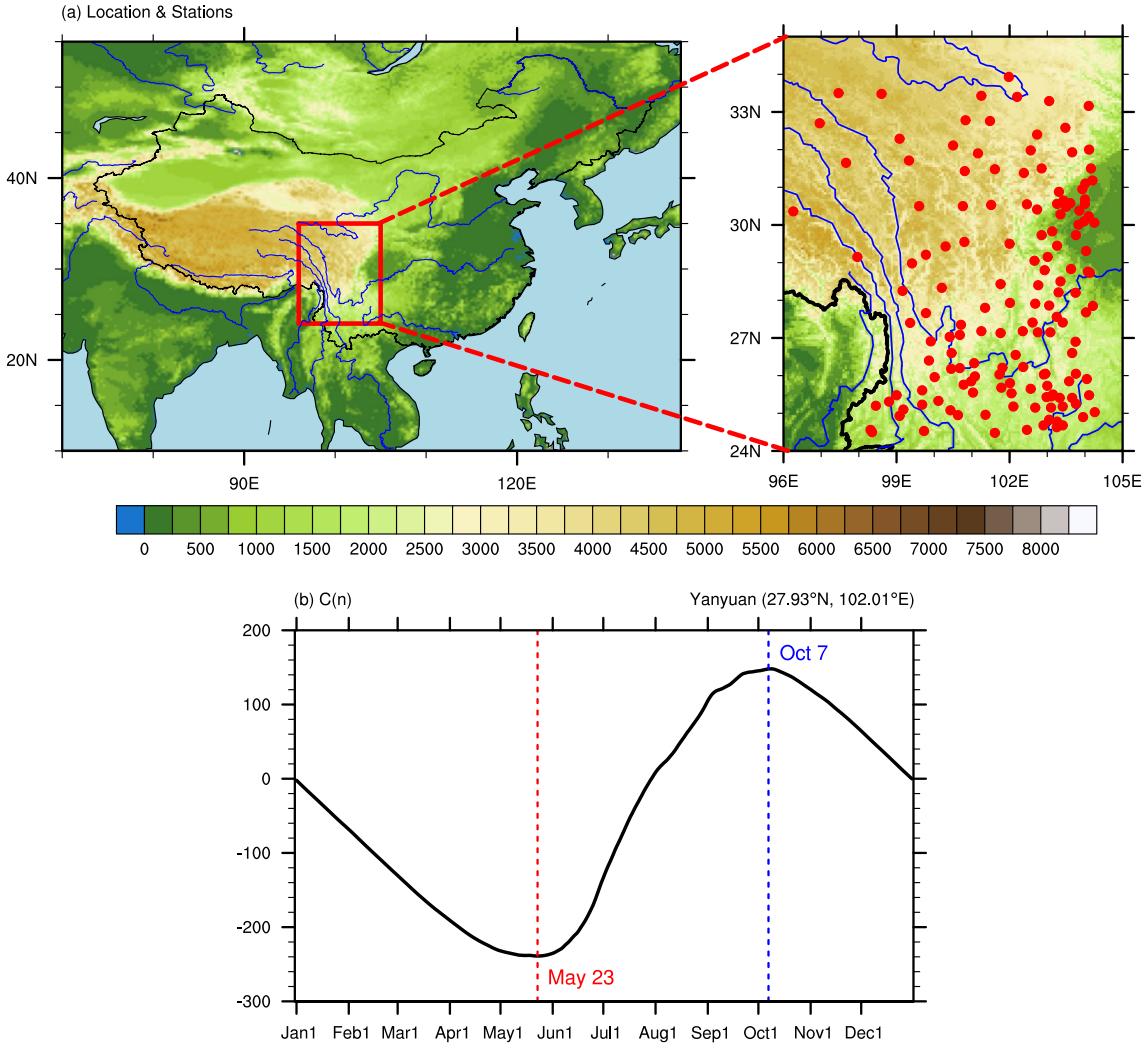

Fig. 1 **a** Topography (shaded; m) from ETOPO1, geographic location of the HM (red box), and distribution of 151 stations (red dots). **b** Cumulative climatological daily precipitation anomaly at Yanyuan station (27.93° N, 102.01° E). The red and blue dashed lines in **b** mark the onset and cessation date of climatological rainy season, respectively

ecosystem consisting of forests, grasslands, rivers, lakes, and glaciers.

The HM is the transition zone between the South Asian and East Asian monsoons, and possess a typical monsoon climate with distinct rainy and drought season. The annual precipitation exceeds 900 mm per year on average, and the rainy season starts from May to October, when the total precipitation accounts for 80–90% of the whole year (Gao et al. 2013; Dong et al. 2018, 2019; Tao et al. 2020). Whereas from November to next April are the drought season with a little precipitation, leading to the high frequency of drought and wildfire occurrence during this period (e.g., Tian et al. 2010, 2014; Wang et al. 2015, 2016; Luo et al. 2019).

During the rainy season, lower-level southwest winds prevail over the HM, connecting the South Asian and East Asian summer monsoons (Zhu et al. 2013; Zhang et al. 2014; Dong et al. 2018). The spatial distribution of climatological rainy season precipitation exhibits a decreasing tendency from the south of HM to the north due to the orographic effects, as the terrain and mountain direction changes (Dong and Duan 1998; Tao et al. 2020). The wet and dry anomalies over the HM during rainy season cooperate well with the changes of South Asian and East Asian summer monsoons (Simmonds et al. 1999; Wang et al. 2001; Zhou et al. 2009; Zhang et al. 2015; Zhu et al. 2016; Tan et al. 2018), and are largely influenced by the tropical air-sea interactions and atmospheric processes at middle and high latitudes (Zhang et al. 2013; Feng et al. 2014; Dong et al. 2018; Tao et al. 2021).

Precipitation is a key variable for the water cycle over the HM (Dong et al. 2016; Wang et al. 2021), and disasters related to precipitation, as drought and wildfire, occur

frequently in this region. Some disastrous droughts around the HM during rainy season are partially related to the precipitation deficiency, as 2006 and 2011 (Li et al. 2011; Wang et al. 2012, 2016). Moreover, less rainy season precipitation reduces the moisture content in live and dead fuels, which contribute to the expand of burned areas during drought season through speeding up the fire spread rate and increasing the flame length (Agee et al. 2002; Chuvieco et al. 2009; Luo et al. 2019). The length of rainy season is one of factors affecting rainy season precipitation over the HM, and are determined by the timing of onset and cessation, which can also directly affect these disasters. The onset (cessation) of rainy season represents the transition from dry (wet) to wet (dry) season. If one year's rainy season begins late (end early), the resulted less precipitation favors the spring (autumn) drought or even prolonged drought from pre-season in this region (Ding and Gao 2020). For example, the droughts in autumn of 2009 and spring-early summer of 2018 are attributed to the late onset and early cessation of HM rainy season, respectively (Zhang et al. 2013; Ding and Gao 2020).

However, there is still no systematic study focusing on the onset and cessation of rainy season over the HM until now. The purpose of present study is to explore the climatology and interannual variation of onset and cessation dates of rainy season over the HM, the associated atmospheric circulation patterns, the involved dynamical mechanisms, and the possible influencing factors. In this study, an objective method is used to determine the timing of onset and cessation in this region for the first time. The obtained results are important to better understand the characteristics of HM regional monsoon climate, and further benefit the ecological environment, social economy, disaster prevention, and mitigation strategies in both local and remote downstream areas. The remainder of the paper is structured as follows: the data and methods are described in Sect. 2. Section 3 investigates the characteristics of climatological onset and cessation date. Section 4 analyses the interannual variations of onset and cessation dates, including the associated circulation anomalies and physical processes. The possible roles of the forcing from the tropics and midlatitudes contributing to the interannual variation of onset and cessation date are explored in Sect. 5. Section 6 presents a concluding summary.

2 Data and methods

2.1 Data

The present study employs observed daily precipitation data from the National Climatic Center of the China Meteorological Administration (NCC/CMA; http://data.cma.cn/en) with 2472 high density national meteorological stations. HM region is defined as a rectangular domain of 24°–35° N and 96°–105° E (Fig. 1a), and the stations with more than 7 consecutive days' default values are eliminated. As a result, 151 stations in HM are selected for analysis. Note that a slight modification of HM region definition does not affect the major conclusions, as that the bootstrapping method is used to test the sensitivity of region selection (figures not shown). The topography data from Earth topography one arc-minute grid (ETOPO1; Amante and Eakins 2009), which uses a 1 arc-minute global relief model of Earth's surface and integrates land topography and ocean bathymetry derived from several sources on a $1' \times 1'$ grid, is used and available at https://www.ngdc.noaa.gov/mgg/global/global.html.

The monthly and daily atmospheric variables used are obtained from Japanese 55-year Reanalysis (JRA-55) on a $1.25° \times 1.25°$ horizontal resolution at 37 pressure levels, compiled by the Japan Meteorological Agency (Kobayashi et al. 2015; Harada et al. 2016). The variables include horizontal winds, vertical pressure velocity, specific humidity, surface pressure, air temperature, geopotential height, and precipitation. The monthly sea surface temperature (SST) data is from NOAA Extended Reconstructed Sea Surface Temperature (ERSST) V5 on a $2° \times 2°$ grid (Smith and Reynolds 2003). The Global Precipitation Climatology Project (GPCP) V2.3 global (land and ocean) precipitation dataset on a $2.5° \times 2.5°$ grid is also used (Adler et al. 2003). The analysis in this study focuses on the period from 1979 to 2018, considering the coincidence of all data's available periods.

2.2 Methods

For daily data, a 7-day running average is applied in order to remove noisy transient synoptic disturbances. For monthly data, the monthly mean climatology is first calculated for the study period. Then, interannual anomalies are computed as the departure from the climatology. Composite, regression, correlation, and empirical orthogonal function (EOF) analysis are used, and the significance level is estimated based on the standard two-tailed Student's t test. To understand the involved dynamical mechanisms, the omega equation and linearized barotropic Rossby wave source are carried out, and these diagnostic methods are introduced on the first occasion when they are used.

The objective method used to determine the onset and cessation date of rainy season is developed by Liebmann and Marengo (2001), which has been widely adopted in other regions (e.g., Liebmann et al. 2008, 2012; Dunning et al. 2016; Li and Sun 2020). To begin with, the period of climatological rainy season is need to be determined. The cumulative climatological daily precipitation anomaly $C(n)$ on day n at each station is defined as:

$$C(n) = \sum_{i=1Jan}^{n} (R_i - \overline{R}), \quad (1)$$

where i starts from 1 January to n, and n ranges from 1 January to 31 December. R_i is the climatological daily precipitation for day i, and $\overline{R}$ is the climatological annual mean precipitation by calculating the annual mean of R_i. For example, the station named as Yanyuan at 27.93° N and 102.01° E is randomly selected, and Fig. 1b shows the $C(n)$ at Yanyuan station. The day of minimum (maximum) in $C(n)$ is the onset (cessation) date of the climatological rainy season, denoted by C_o (C_c). The C_o and C_c for Yanyuan are 23 May and 7 October, respectively (Fig. 1b).

Then the onset and cessation date of rainy season for each year are determined by calculating the cumulative daily precipitation anomaly on day N:

$$A(N) = \sum_{j=C_o-50}^{N} \left(P_j - \overline{R}\right), \quad (2)$$

where P_j is the daily precipitation for day j of the given year, and N ranges from $C_o - 50$ to $C_c + 50$. Note that the 50 days' extension before and after C_o and C_c is applicable to the region with single rainy season per year (Dunning et al. 2016; Li and Sun 2020). The day of minimum (maximum) in $A(N)$ is the onset (cessation) date of the rainy season for the given year. The onset (cessation) date for the HM is defined as that more than 60% of the stations in this region have started (ended) the rainy season.

3 Climatology of onset and cessation date

3.1 Characteristics of rainy season

Figure 2 shows the onset date, cessation date, length, and total precipitation of climatological rainy season over the HM. For all stations over the HM, the climatological onset dates are not geographically homogeneous, and about 70% stations in the HM start the rainy season between 30 April and 24 May (Fig. 2a). The rainy season starts earlier in the western HM, followed by the eastern, northern, and southern HM, and the latest onset dates are concentrated in the central HM. There is a little difference in the climatological cessation dates among the stations over the HM, and about 70% stations in the HM end the rainy season between 6 and 15 October, although that the rainy season ends slightly earlier in the eastern HM (Fig. 2b).

As a result, the length of climatological rainy season depends largely on the climatological onset date, as the highly resembling spatial distribution between them (Fig. 2a, c). The climatological rainy season for the HM starts at 14 May and ends at 12 October, and its length is 151 days, consistent with the previous definition of the rainy season from May to September over the HM based on the climatological monthly precipitation (Gao et al. 2013; Dong et al. 2018, 2019; Tao et al. 2020). The climatological total precipitation exhibits a decreasing tendency from the southern to northern HM (Fig. 2d), indicating the more crucial role of the precipitation rate rather than length of rainy season. The climatological precipitation rate seems to be controlled by the orographic effects, which force the incoming moisture to rise on the windward slope in the southern HM, while less moisture and weak orographically forced mechanical lifting are in the Northern HM (Tao et al. 2020).

3.2 Associated climatological atmospheric circulation

In this subsection, the associated climatological atmospheric circulation for 30 days before and after the climatological onset and cessation date of HM are compared. During the pre-30 days of climatological onset date, the southwesterly moisture transport appears in the Bay of Bengal (BOB; Fig. 3a). The southwesterlies are significantly intensified and extend westward to the Arabian Sea (AS) after the onset of climatological rainy season, denoting the onset of Indian summer monsoon (ISM; Fig. 3b). Two moisture transport channels are emerged: one goes through the South China Sea to the northwest Pacific (NWP), and another goes all the way to the HM. The two channels can be also seen in the differences between the post- and pre-30 days (Fig. 3c), and the former channel corresponds with the eastward shift of NWP subtropical high. Note that the moisture is mainly confined at lower levels, so the spatial distribution of 850 hPa winds resembles that of moisture flux (Figs. 3a–c, 4a–c). The onset of rainy season in the HM is triggered by the strengthened southerly anomalies at the southwest side of HM, accompanying by the moisture convergence and upward motions over the HM (Figs. 3c, 4c). The 200 hPa subtropical jet shifts northward from pre- to post-30 days (Fig. 5a, b), and the anticyclonic wind anomalies with high geopotential height anomalies are observed, indicating the establishment of South Asian high (Fig. 5c).

The composite maps for the cessation of climatological rainy season are almost opposite to the onset. The moisture transported by the southwesterlies over the north Indian Ocean (IO) during the pre-30 days of climatological cessation date are replaced by northeasterlies during the post-30 days (Figs. 3d, e, 4d, e). Accompanied with the westward shift of NWP subtropical high, the east wind anomalies originate from the NWP and extend to the AS in the differences between two periods, and the northerly anomalies at the southwest side of HM lead to the moisture divergence and downward motions over the HM, indicating the cessation

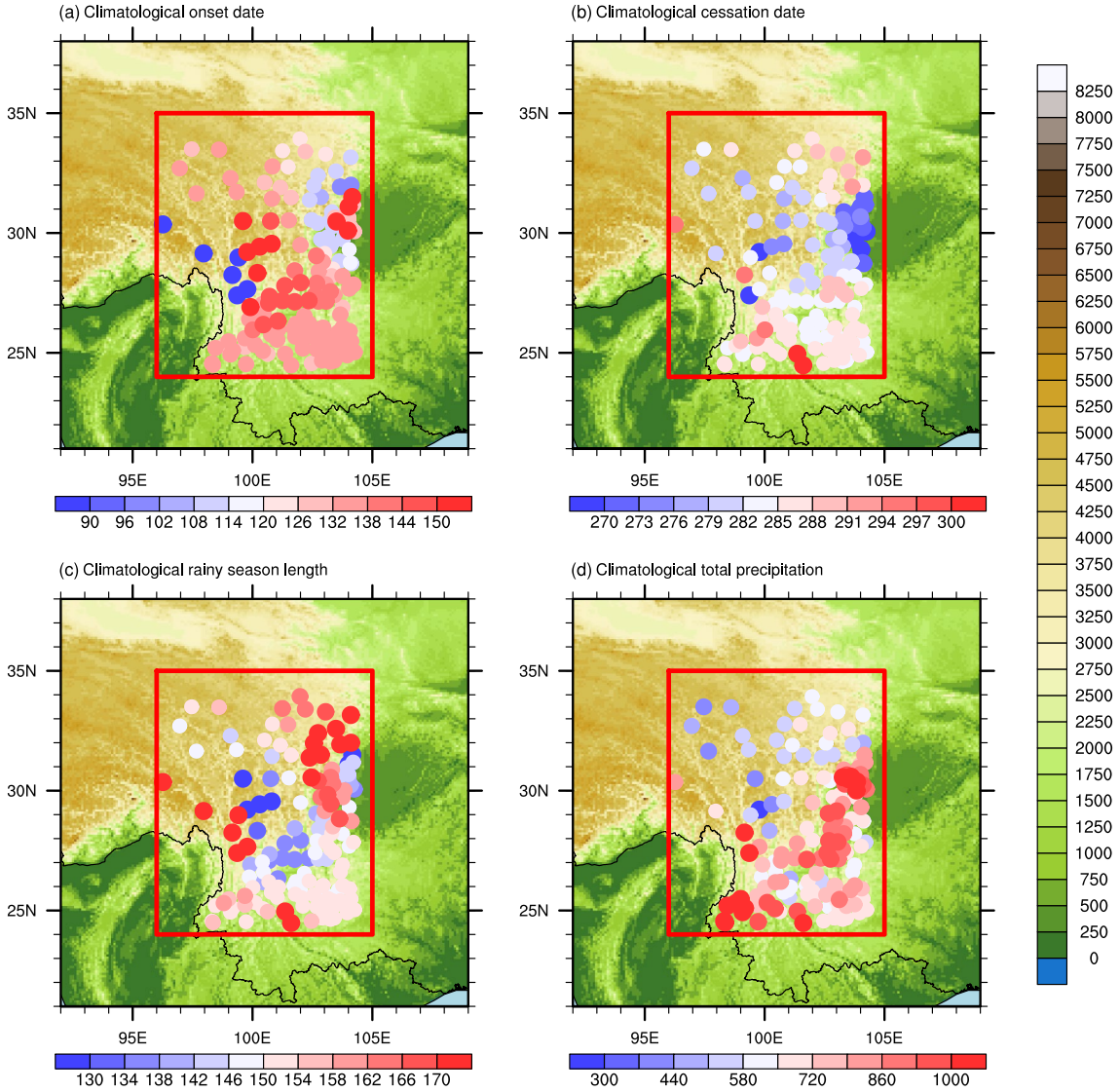

Fig. 2 **a** Onset date (day of the year), **b** cessation date (day of the year), **c** length (day), and **d** total precipitation (mm) of climatological rainy season over the HM

of climatological rainy season (Figs. 3f, 4f). The 200 hPa subtropical jet shifts southward from pre- to post-30 days (Fig. 5d, e), and the South Asian high weakens and withdraws associated with the cyclonic wind anomalies and low geopotential height anomalies (Fig. 5c). Note that although the 30 days' averaged results are present here, the climatological onset and cessation related key large-scale circulation, as ISM, 200 hPa subtropical jet, and South Asia high, are indeed continuously changing from pre- to post-30 days (figures not shown).

4 Interannual variation of onset and cessation dates

The evolution of onset and cessation dates in the HM from 1979 to 2018 are shown in Fig. 6. The onset dates range from 30 April (2007) to 8 June (2015), and the 40-year averaged onset date is 20 May, which is 6 days later than the climatological onset date. The cessation dates range from 26 September (1981) to 4 November (2008), and the 40-year averaged cessation date is 14 October, which is 2 days later than the climatological cessation date. Both onset and cessation dates exhibit strong interannual variability with the standard deviation of 12 and 10 days, respectively. If the time series of onset dates are normalized and selected based on the criterion of one standard

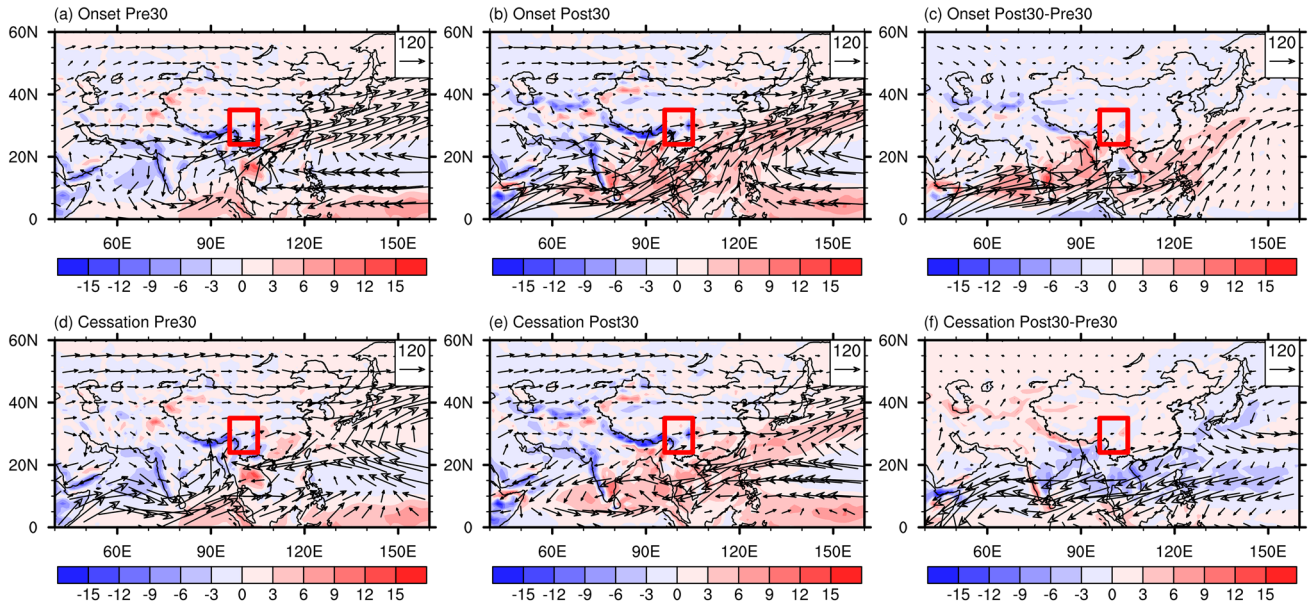

Fig. 3 Composite of column-integrated moisture flux (vector; kg s^{-1} m^{-1}) and moisture divergence (shaded; mm) for **a** 30 days before climatological onset date, **b** 30 days after climatological onset date, and **c** their differences. **d**, **e**, and **f** are same as **a**, **b**, and **c**, but for climatological cessation date

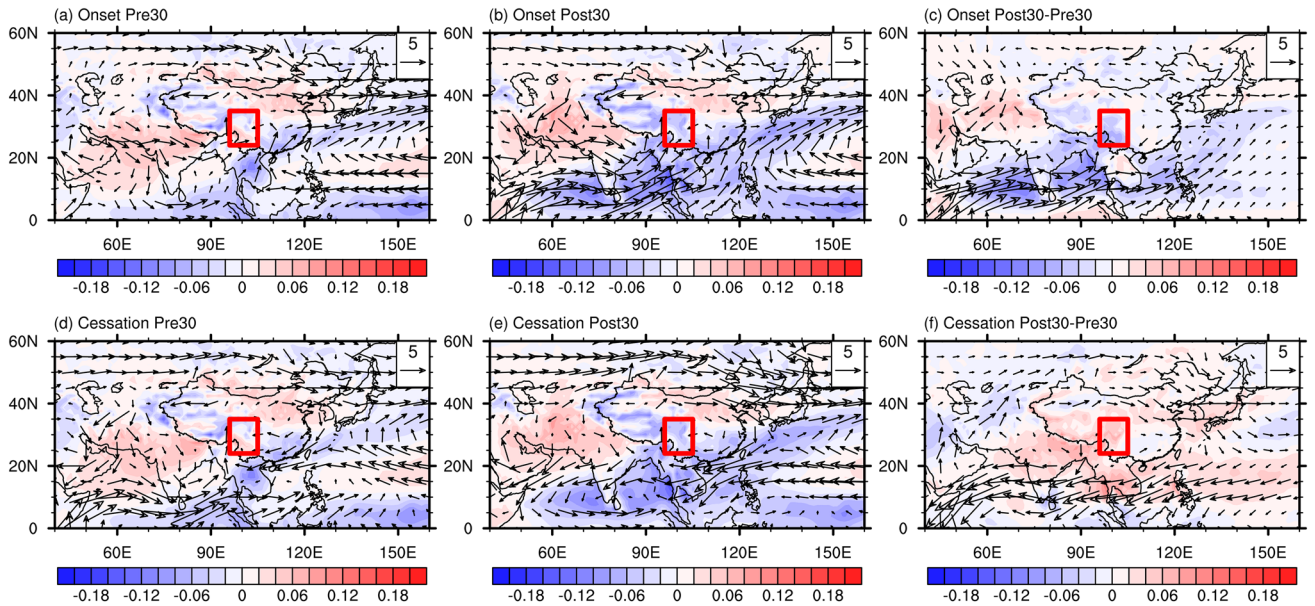

Fig. 4 As Fig. 3, but for 850 hPa winds (vector; m s^{-1}) and 400 hPa vertical velocity (shaded; Pa s^{-1})

deviation, the early onset dates are from 30 April to 7 May, and late onset dates are from 29 May to 8 June. Selecting based on one standard deviation to the normalized cessation dates, the early cessation dates are from 26 September to 3 October, and late cessation dates are from 24 October to 4 November. There are nearly 30 days' difference between the early and late onset or cessation dates, and the atmospheric conditions during the nearly 30 days plays a crucial role in determining the onset or cessation dates of HM rainy season. Thus, the monthly data in May and October are used to explore the interannual variation of onset and cessation dates, including the associated atmospheric circulation anomalies and the involved dynamical mechanisms. The shorter periods as the subsets of May and October by using daily data are also tried and do not alter the major conclusions.

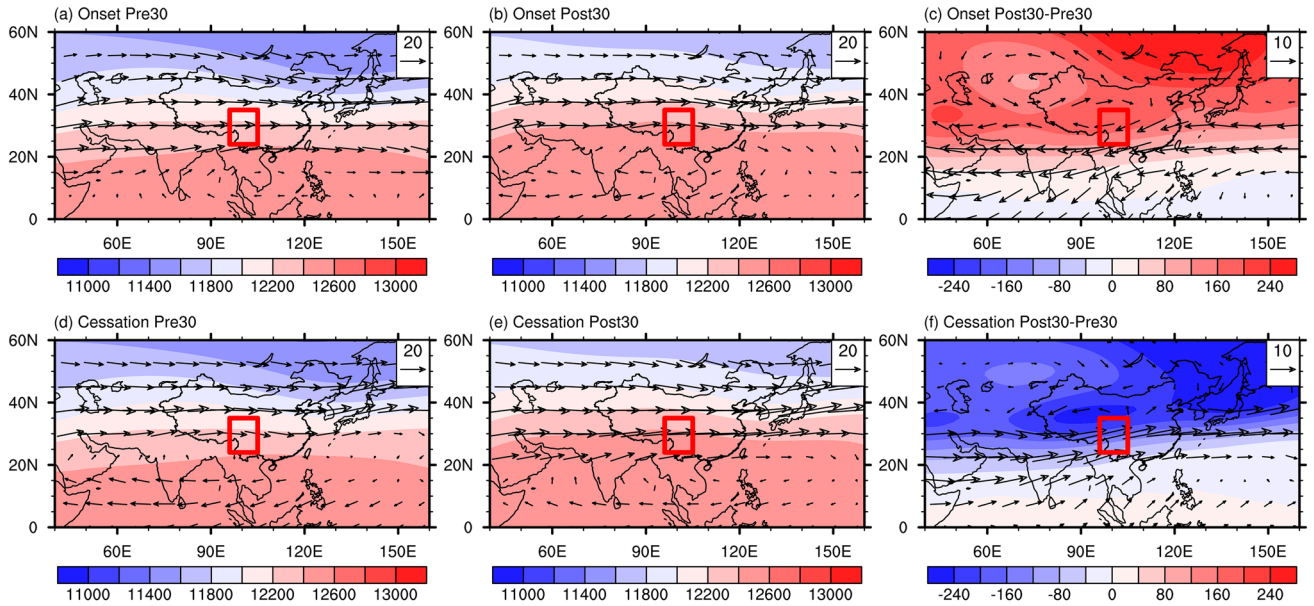

Fig. 5 As Fig. 3, but for 200 hPa winds (vector; m s^{-1}) and 200 hPa geopotential height (shaded; gpm)

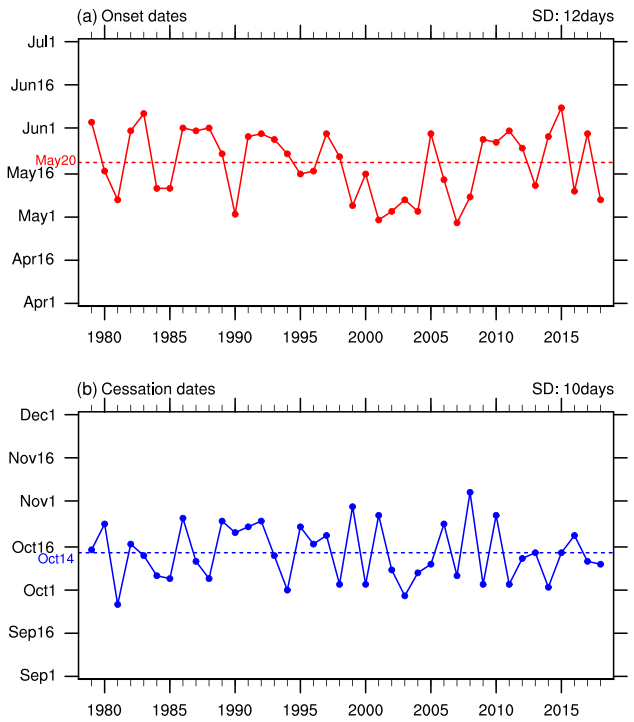

Fig. 6 The evolution of **a** onset and **b** cessation dates in the HM for the period of 1979–2018. The red dashed line in **a** marks the climatological onset date, and the blue dashed line in **b** marks the climatological cessation date. The standard deviation of each time series is on the top right corner of each panel

4.1 Associated atmospheric circulation anomalies

Figure 7a, c, e present the regression of column-integrated moisture flux and moisture divergence, 850 hPa winds and 400 hPa vertical velocity, and 200 hPa winds and 200 hPa geopotential height in May with respect to the normalized onset dates over the HM, respectively. Corresponding to the late onset, notable anomalous moisture divergence and downward motions extend from the north IO to HM, and the northeasterly wind anomalies at lower levels are observed over the north IO (Fig. 7a, c). On one hand, the northeasterly wind anomalies delay the advance of moisture transported by ISM. On the other hand, the northeasterly wind anomalies cooperate with the westerly wind anomalies at the north flank of the anomalous anticyclone over the NWP and the topography around the HM, leading to the anomalous moisture divergence and downward motions. Besides, the distribution of upper-level circulation anomalies manifests a dipole pattern around the HM, characterized by negative geopotential height anomalies with a closed cyclonic circulation on the north side of the AS and a positive geopotential height anomaly center with an anomalous anticyclone over the central and southern China (Fig. 7e).

Figure 7b, d, f show the regressed atmospheric circulation anomalies onto the normalized cessation dates. In accord with late cessation, the well-defined anomalous moisture convergence, upward motions, and moist southerly flow are found on the south side of HM (Fig. 7b, d). The anomalous lower-level southerlies are located at the east flank of cyclonic wind anomalies over the north IO and the west flank of anticyclonic wind anomalies over the NWP, implying the anomalous transport of moisture from the warm pool. At 200 hPa, a dipole pattern, which shifts westward and is

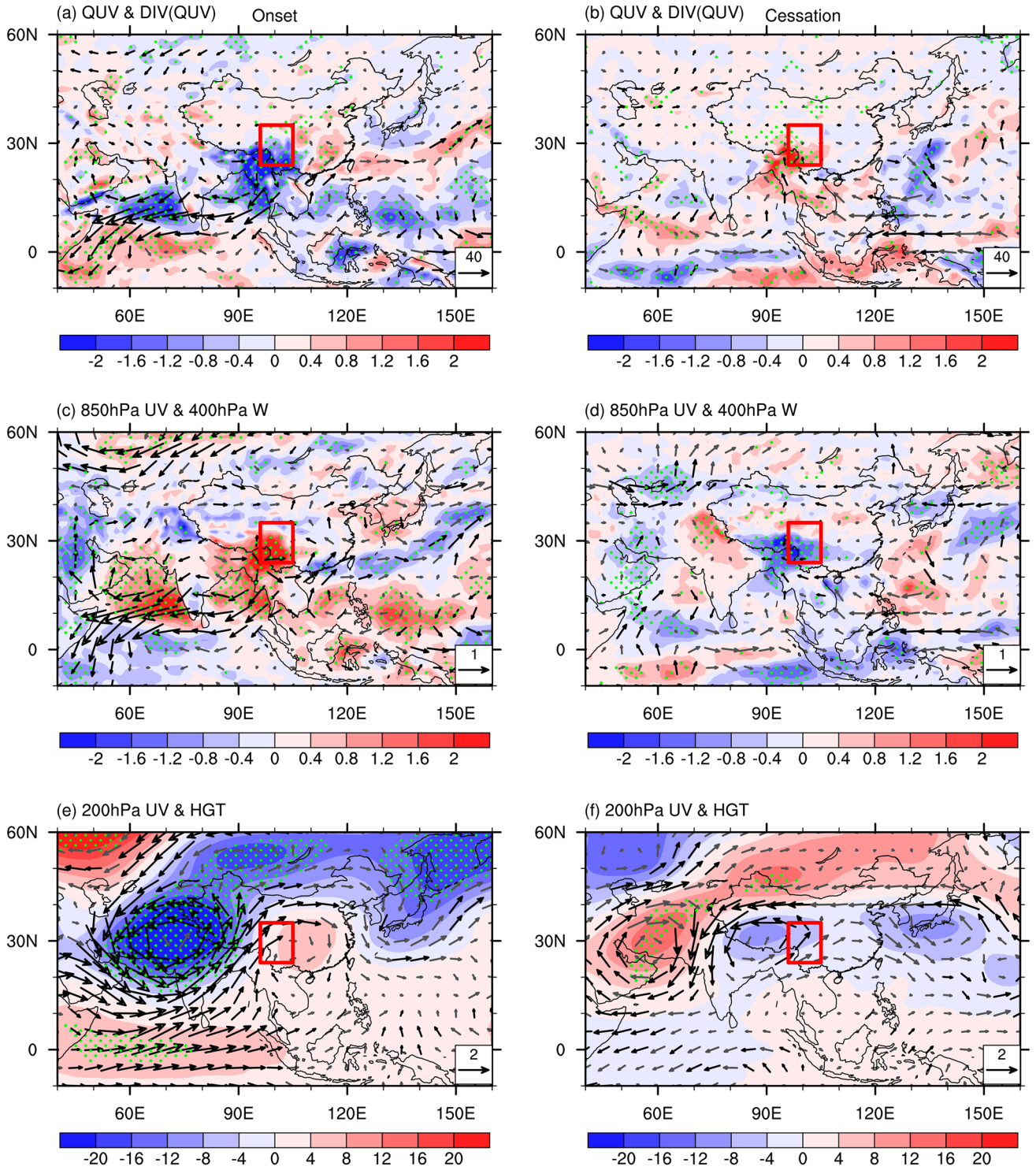

Fig. 7 Regression of **a** column-integrated moisture flux (vector; kg s^{-1} m^{-1}) and moisture divergence (shaded; mm), **c** 850 hPa winds (vector; m s^{-1}) and 400 hPa vertical velocity (shaded; 10^2 Pa s^{-1}), **e** 200 hPa winds (vector; m s^{-1}) and 200 hPa geopotential height (shaded; gpm) in May with respect to the normalized onset dates over the HM. **b**, **d**, and **f** are as **a**, **c**, and **e**, but in October with respect to the normalized cessation dates over the HM. Green dots and black bold vectors indicate that the confidence level reaches 90%

opposite in zonal direction compared with the results related to the onset dates, develops over the Iran and TP (Fig. 7f). It is worth noting that the vertical motions are important to the precipitation and have a close relationship with the circulation at lower and upper levels. Therefore, the omega equation is used to diagnose the vertical motion anomalies for interannual variation of onset and cessation dates in next subsection (Kosaka and Nakamura 2010; Wei et al. 2014; Zhao et al. 2015; Hu et al. 2017; Dong et al. 2018; Tao et al. 2021).

4.2 Omega equation analysis

The anomalous vertical motions can be diagnosed as:

$$\begin{aligned}\omega' = &\left(\nabla^2 + \frac{f^2}{\sigma^2}\frac{\partial^2}{\partial P^2}\right)^{-1}\frac{R}{\sigma P}\nabla^2\left(\overline{\mathbf{V}}\cdot\nabla T' + \mathbf{V}'\cdot\nabla\overline{T}\right)\\ &+\left(\nabla^2 + \frac{f^2}{\sigma^2}\frac{\partial^2}{\partial P^2}\right)^{-1}\frac{f}{\sigma}\frac{\partial}{\partial P}\left[\overline{\mathbf{V}}\cdot\nabla\zeta' + \mathbf{V}'\cdot\nabla\left(f+\overline{\zeta}\right)\right]\\ &-\left(\nabla^2 + \frac{f^2}{\sigma^2}\frac{\partial^2}{\partial P^2}\right)^{-1}\frac{R}{\sigma P c_p}\nabla^2 Q,\end{aligned} \tag{3}$$

where the overbars denote the climatology state, the primes denote regressed anomalies, ω is vertical pressure velocity, $\sigma = \frac{R}{P}\left(\frac{RT}{c_p P} - \frac{d\overline{T}}{dP}\right)$ is static stability, f is Coriolis parameter, P is air pressure, $\mathbf{V} = (u, v)$ is the horizontal wind components, ζ is relative vorticity, R is gas constant, T is air temperature, c_P is specific heat at constant pressure, and Q is diabatic heating. The terms on the right side of the equation denote the anomalous vertical motions due to the horizontal temperature advection (ω'_{therm}), the vertical difference of horizontal vorticity advection (ω'_{vor}), and the diabatic heating (ω'_{Q}), respectively. ω'_{therm} and ω'_{vor} can be further decomposed and represented as the contribution of $\overline{u}\frac{\partial T'}{\partial x}$, $\overline{v}\frac{\partial T'}{\partial y}$, $u'\frac{\partial\overline{T}}{\partial x}$, $v'\frac{\partial\overline{T}}{\partial y}$, $\overline{u}\frac{\partial\zeta'}{\partial x}$, $\overline{v}\frac{\partial\zeta'}{\partial y}$, $u'\frac{\partial\overline{\zeta}}{\partial x}$, $v'\frac{\partial\overline{\zeta}}{\partial y}$, and $v'\frac{\partial f}{\partial y}$:

$$\omega'_{therm} = \left(\nabla^2 + \frac{f^2}{\sigma^2}\frac{\partial^2}{\partial P^2}\right)^{-1}\frac{R}{\sigma P}\nabla^2\left(\overline{u}\frac{\partial T'}{\partial x} + \overline{v}\frac{\partial T'}{\partial y} + u'\frac{\partial\overline{T}}{\partial x} + v'\frac{\partial\overline{T}}{\partial y}\right), \tag{4}$$

$$\begin{aligned}\omega'_{vor} = &\left(\nabla^2 + \frac{f^2}{\sigma^2}\frac{\partial^2}{\partial P^2}\right)^{-1}\frac{f}{\sigma}\frac{\partial}{\partial P}\\ &\left(\overline{u}\frac{\partial\zeta'}{\partial x} + \overline{v}\frac{\partial\zeta'}{\partial y} + u'\frac{\partial\overline{\zeta}}{\partial x} + v'\frac{\partial\overline{\zeta}}{\partial y} + v'\frac{\partial f}{\partial y}\right).\end{aligned} \tag{5}$$

The maximum ascending and subsiding anomalies averaged over the HM related to onset and cessation dates are at 400 hPa respectively (figure not shown), and Fig. 8 shows the diagnosed results of omega equation at 400 hPa in regional average. ω_Q is the largest contribution both for onset and cessation dates (Fig. 8), and is considered as the circulation-precipitation feedback (Hu et al. 2017; Tao et al. 2020).

For onset dates, ω'_{therm} contributes more to the anomalous downward motions over the HM than ω'_{vor}, and further decomposition of ω'_{therm} reveals the importance of the anomalous temperature advected by the climatology zonal winds ($\overline{u}\frac{\partial T'}{\partial x}$) and the climatology temperature advected by the anomalous meridional winds ($v'\frac{\partial\overline{T}}{\partial y}$), although that the vertical motion anomalies contributed by $v'\frac{\partial\overline{T}}{\partial y}$ is about half of $\overline{u}\frac{\partial T'}{\partial x}$ (Fig. 8a). Figure 9a, b present the spatial distribution of $\overline{u}\frac{\partial T'}{\partial x}$ and $v'\frac{\partial\overline{T}}{\partial y}$ at 400 hPa, respectively. $\overline{u}\frac{\partial T'}{\partial x}$ related negative temperature advection occupies the HM (Fig. 9a), while $v'\frac{\partial\overline{T}}{\partial y}$ related negative temperature advection only appears in the southeast corner of HM (Fig. 9b). The spatial distribution of $\overline{u}\frac{\partial T'}{\partial x}$ corresponding climatological circulation and anomalous air temperature and $v'\frac{\partial\overline{T}}{\partial y}$ corresponding anomalous circulation and climatological air temperature at 400 hPa are shown in Fig. 9c, d, respectively, to better understand the physical processes related to the negative temperature advection. On one hand, the air temperature exhibits negative anomalies on the north side of the AS, and the climatological zonal winds advect the anomalous cold air to the HM (Fig. 9c). On the other hand, the northwesterly anomalies advect climatological relative cold air from high latitudes to the southeast corner of HM (Fig. 9d).

For cessation dates, ω'_{therm} and ω'_{vor} are comparable in the contribution of the anomalous upward motions over the HM. Further analysis finds that the climatology temperature advected by the anomalous meridional winds ($v'\frac{\partial\overline{T}}{\partial y}$) and the anomalous vorticity advected by the climatology zonal winds ($\overline{u}\frac{\partial\zeta'}{\partial x}$) are dominant in ω'_{therm} and ω'_{vor}, respectively. $v'\frac{\partial\overline{T}}{\partial y}$ related positive temperature advection corresponds well with the ascending anomalies around the HM (Fig. 10a), and the anomalous southwesterly anomalies advect climatological warm air form the tropics to the HM (Fig. 10c). A clear dipole structure of vorticity advection can be seen at upper levels (Fig. 10b). The positive vorticity advection around the HM decreases with increasing pressure level, and the resulting negative vertical difference of vorticity advection matches well with the ascending anomalies, which peak at around 400 hPa. Moreover, the upper-level dipole structure of vorticity advection originates form the anomalous vorticity dipole cooperating with the climatological zonal westerlies (Fig. 10d).

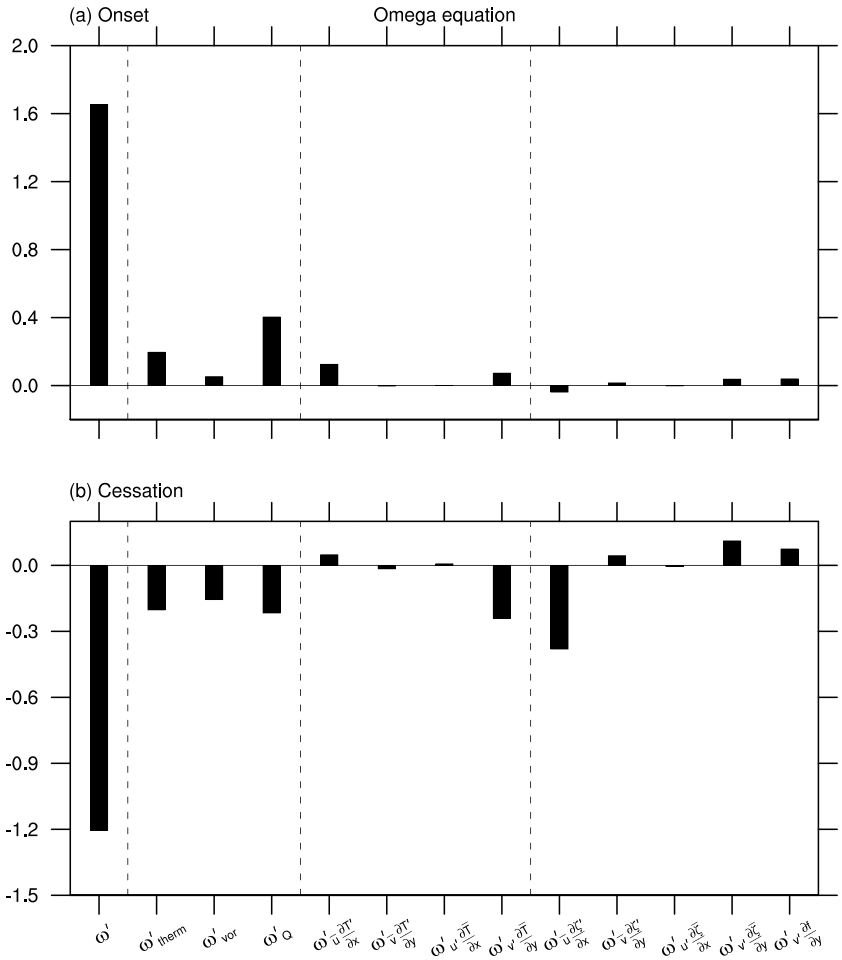

Fig. 8 Omega equation analysis of **a** onset dates and **b** cessation dates regressed vertical pressure velocity anomalies (10^{-2} Pa s^{-1}) in May and October over the HM, respectively

5 Roles of atmospheric wave train and SST

By using omega equation, the previous section investigates the physical processes involved in the vertical motion anomalies related to the interannual variation of onset and cessation dates, and reveals the close relationship between anomalous circulation and vertical motions. Note that $\overline{u}\frac{\partial T'}{\partial x}$ for onset dates is partially attribute to the distribution of anomalous 400 hPa air temperature, which is close to the distribution of anomalous 200 hPa circulation (Figs. 7e, 9c), indirectly reflecting the connection between anomalous circulation and vertical motions. In this section, the possible factors from the tropics and midlatitudes inducing the anomalous circulation and vertical motions are explored.

5.1 SST and lower-level circulation anomalies

Figure 11a, c present the onset dates regressed SST and precipitation anomalies in May, respectively. A tripole structure of SST anomalies is exhibited over the Indo-Pacific sector with the warming over the equatorial central and eastern Pacific (CEP), north IO, and southwest IO, and cooling over the western Pacific and most of the northern and southern subtropical Pacific (Fig. 11a). The SST anomalies over the west IO feature the clear meridional SST gradient, which favors a C-shaped pattern of wind anomalies, with anomalous northeasterlies north and northerlies south of the equator as a result of the Coriolis force (Fig. 7c; Wu et al. 2008; Du et al. 2009; Wu and Yeh 2010). Consistent with the anomalous wind response, there are wet anomalies over the southwest IO and dry anomalies over the north IO (Fig. 11c), indicating that the southwest IO warming dominantly excites the C-shaped wind anomalies. While the north IO warming is the passive response of local anomalous northeasterlies, which are opposite to the southwest monsoon and further reduce the latent heat loss form the ocean (Wu et al. 2008; Du et al. 2009; Wu and Yeh 2010). Besides, the anomalous anticyclone over the NWP is triggered as a Rossby wave response to the local cooling and by the

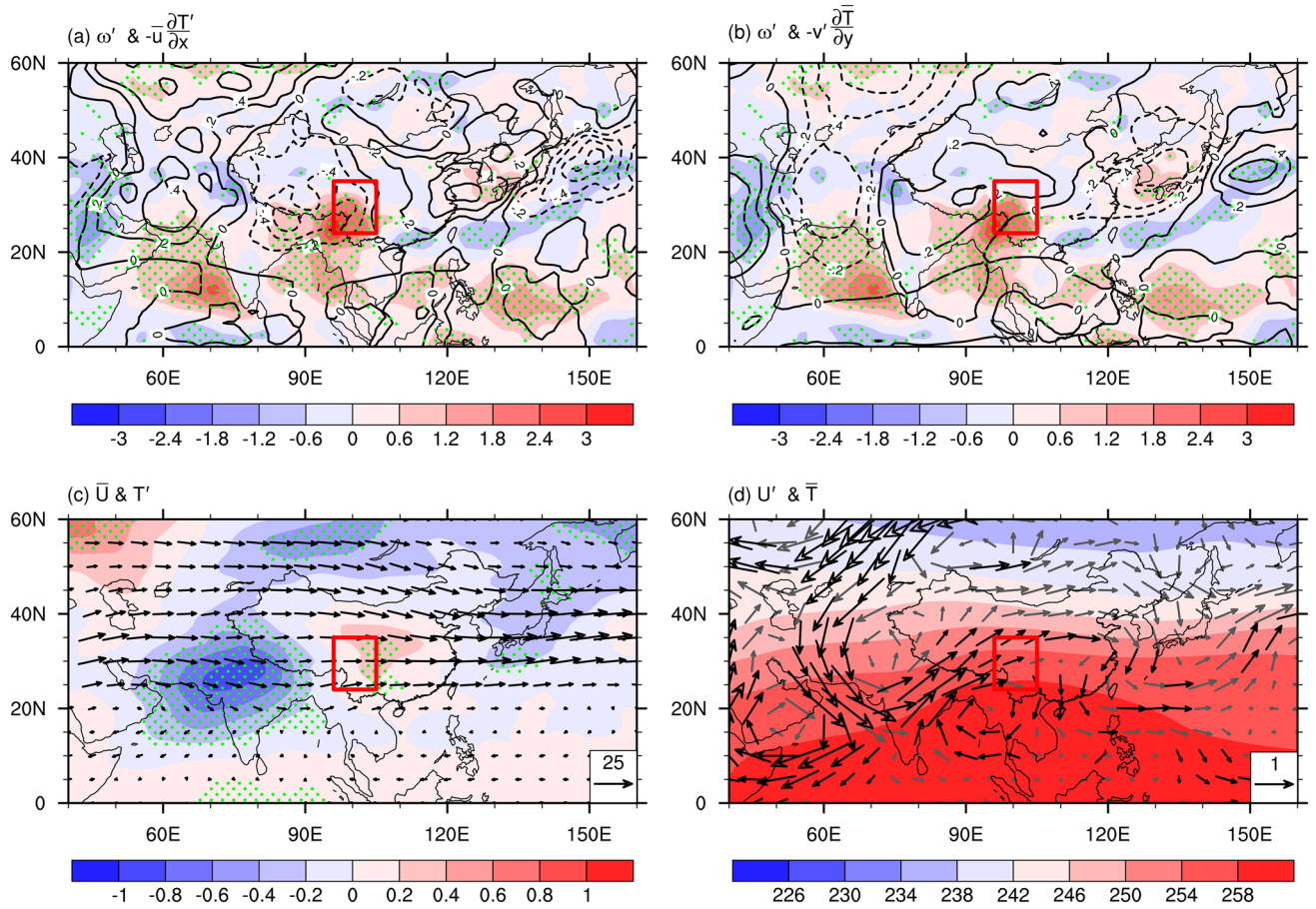

Fig. 9 **a** The anomalous temperature advected by the climatology zonal winds (contour; 10^{-5} K s^{-1}) and **b** the climatology temperature advected by the anomalous meridional winds (contour; 10^{-5} K s^{-1}) in May for onset dates. The shaded in **a** and **b** are the onset dates regressed 400 hPa vertical pressure velocity anomalies (10^{-2} Pa s^{-1}), which are same as the shaded in Fig. 7c. **c** Climatology of 400 hPa winds (vector; m s^{-1}) in May and regression of 400 hPa air temperature (shaded; K) in May with respect to the normalized onset dates over the HM. **d** Regression of 400 hPa winds (vector; m s^{-1}) in May with respect to the normalized onset dates over the HM and climatology of 400 hPa air temperature (shaded; K) in May. Green dots and black bold vectors indicate that the confidence level reaches 90%

remote teleconnection of the El Niño-like CEP warming (Wang et al. 2000; Wu et al. 2017; Tao et al. 2019).

The cessation dates regressed SST and precipitation anomalies in October are shown in Fig. 11b, d, respectively. Significant negative SST anomalies appear over the equatorial west and southeast IO (Fig. 11b), while the strong negative precipitation anomalies are only observed over the equatorial west IO (Fig. 11d). The climatological SST in October is higher over the equatorial west IO than southeast IO (Fig. 11b), thus the anomalous cooling is easier to decrease the convection over the equatorial west IO (Fig. 11d). In response to the equatorial west IO cooling, the zonal circulation is adjusted with lower-level westerly and upper-level easterly anomalies over the equatorial IO (Fig. 7d, f), causing the anomalous moisture convergence, upward motions, and positive precipitation from the equatorial east IO to Maritime Continent (Figs. 7b, d, 11d). Furthermore, the cyclonic wind anomalies over the northeast IO and easterly anomalies over the western Pacific are triggered as the Rossby and Kelvin wave response to the positive precipitation anomalies respectively, and the two flow channels are merged and turn into southerly anomalies on the south side of HM. Note that the precipitation anomalies from GPCP V2.3 highly resemble those from JRA-55, confirming the reliability of using reanalysis dataset for analysis.

5.2 Atmospheric wave train and upper-level circulation anomalies

Figure 12 shows the 200 hPa geopotential height anomalies and 200 hPa horizontal component of wave activity fluxes

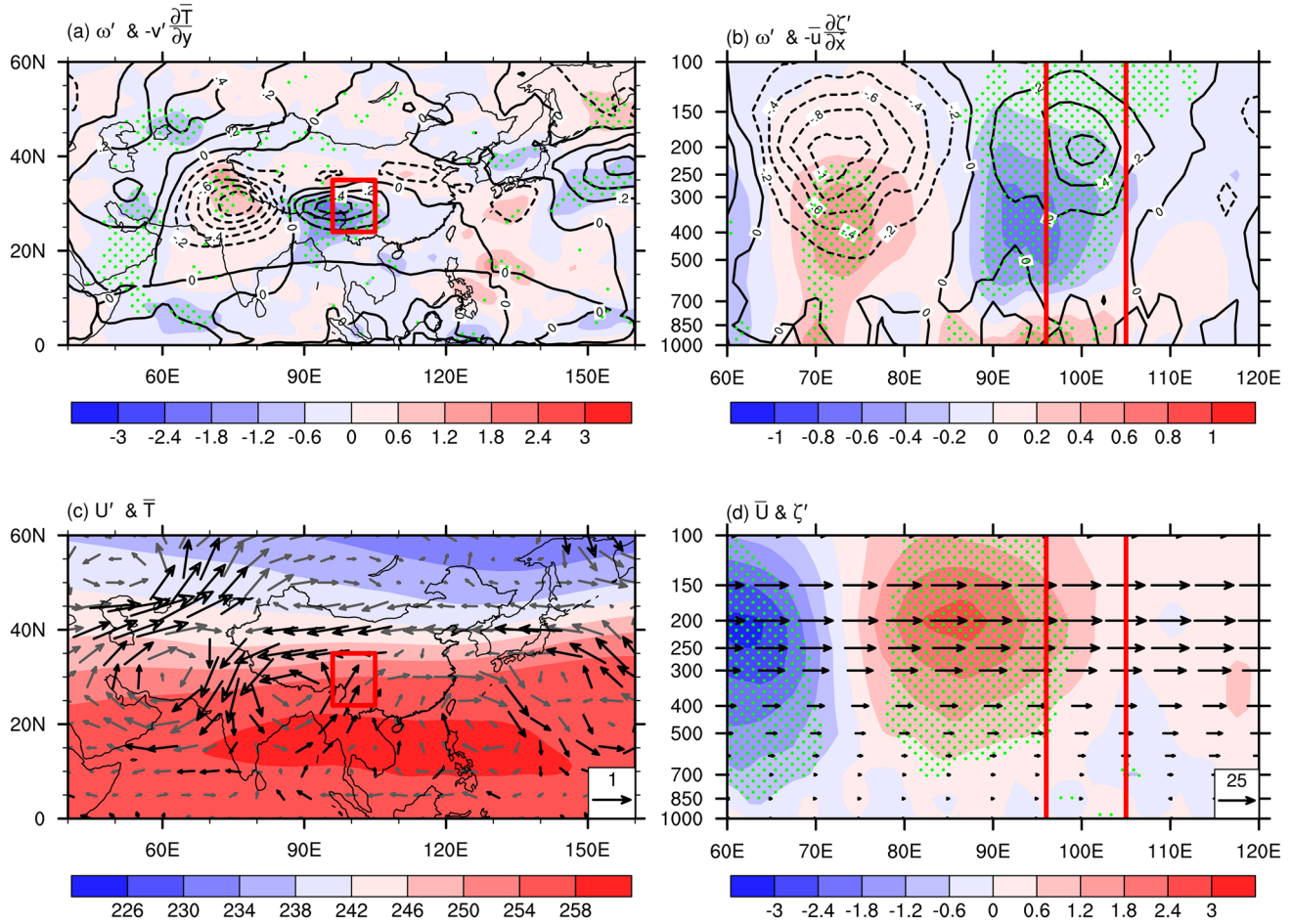

Fig. 10 **a** The climatology temperature advected by the anomalous meridional winds (contour; 10^{-5} K s^{-1}) in October and the cessation dates regressed 400 hPa vertical pressure velocity anomalies (10^{-2} Pa s^{-1}) in October, which are same as the shaded in Fig. 7d. **b** Latitude–height profile of the anomalous vorticity advected by the climatology zonal winds (contour; 10^{-10} s^{-2}) in October and regression of vertical pressure velocity (10^{-2} Pa s^{-1}) in October with respect to the normalized cessation dates over the HM by calculating meridionally averaged in 20°–30° N. **c** Regression of 400 hPa winds (vector; m s^{-1}) in October with respect to the normalized cessation dates over the HM and the climatology of 400 hPa air temperature (shaded; K) in October. **d** Latitude–height profile of the climatology of zonal winds (vector; m s^{-1}) in October and regression of vorticity (shaded; 10^{-6} s^{-1}) in October with respect to the normalized cessation dates over the HM by calculating meridionally averaged in 20°–30° N. Green dots and black bold vectors indicate that the confidence level reaches 90%, and red lines in **b** and **d** denote the zonal boundaries of HMs

related to onset and cessation dates over Eurasia, which covers the larger spatial range than Fig. 7. For onset dates, two wave trains are observed: one is trapped along the subtropical Asian jet stream, and the other is emanating from the British Isles, crossing northern Scandinavia, and going through Mongolia to China (Fig. 12a). The whole structure over Eurasia highly resembles the Silk Road pattern (SRP; Lu et al. 2002; Enomoto et al. 2003; Kosaka et al. 2009), and the pattern correlation coefficient between them is 0.70 (Fig. 12a, c). The SRP index is defined as the first EOF mode of 200 hPa meridional winds in the domain of 10°–50° N, 30°–110° E, and the SRP index in May is correlated with the time series of onset dates at 0.62 reaching the 99% confidence level, indicating the contribution from SRP. For cessation dates, the 200 hPa geopotential height anomalies and wave activity fluxes show the similar spatial distribution but with the opposite phase, the weaker intensity, and the slight shift of anomaly center position compared with these of onset dates (Fig. 12a, b). The pattern correlation coefficient of 200 hPa geopotential height anomalies related to cessation dates and SRP index in October is 0.63 (Fig. 12b, d), and the correlation coefficient between two time series is 0.43 reaching the 99% confidence level.

Note that the closed anomaly center of 200 hPa geopotential height on the north side of the AS is especially stronger than other centers both for onset and cessation dates, as well as the accompanied wave activity fluxes

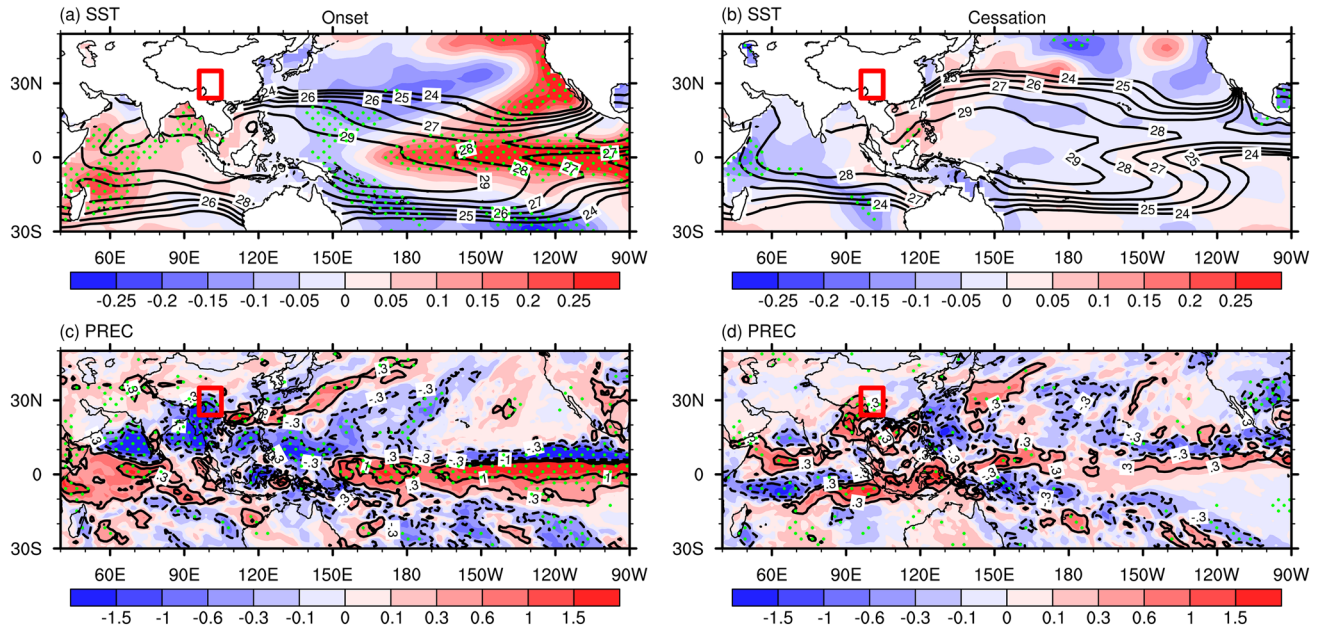

Fig. 11 Regression of **a** SST (shaded; K) from ERSST V5 and **c** precipitation (shaded; mm) from JRA-55 in May with respect to the normalized onset dates over the HM. **b** and **d** are as **a** and **c**, but in October with respect to the normalized cessation dates over the HM. Contours in **a** and **b** are the climatology of SST (24, 25, 26, 27, 28, 29 K) in May and October respectively, and contours in **c** and **d** are the regression of precipitation (± 0.3 mm, ± 1 mm; negative contours are dashed) from GPCP V2.3 in May and October with respect to the normalized onset and cessation dates over the HM respectively. Green dots indicate that the confidence level reaches 90%

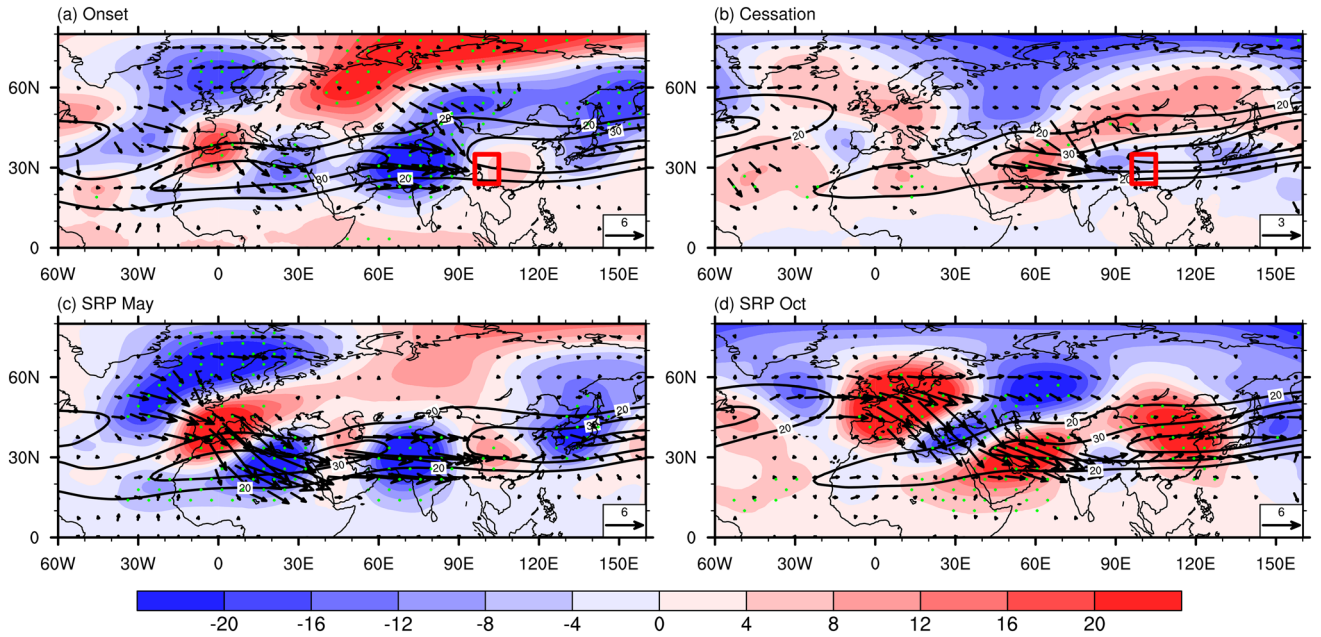

Fig. 12 Regression of 200 hPa geopotential height (shaded; gpm) in May and October with respect to the normalized **a** onset and **b** cessation dates over the HM, and SRP index in **c** May and **d** October, respectively, and 200 hPa horizontal component of wave activity fluxes (vector; $m^2\ s^{-2}$), and climatology of 200 hPa zonal winds (contour; $m\ s^{-1}$). Green dots indicate that the confidence level reaches 90%, and vectors with magnitudes less than 0.1 $m^2\ s^{-2}$ are omitted, and only contours with values greater than 20 $m\ s^{-1}$ are plotted

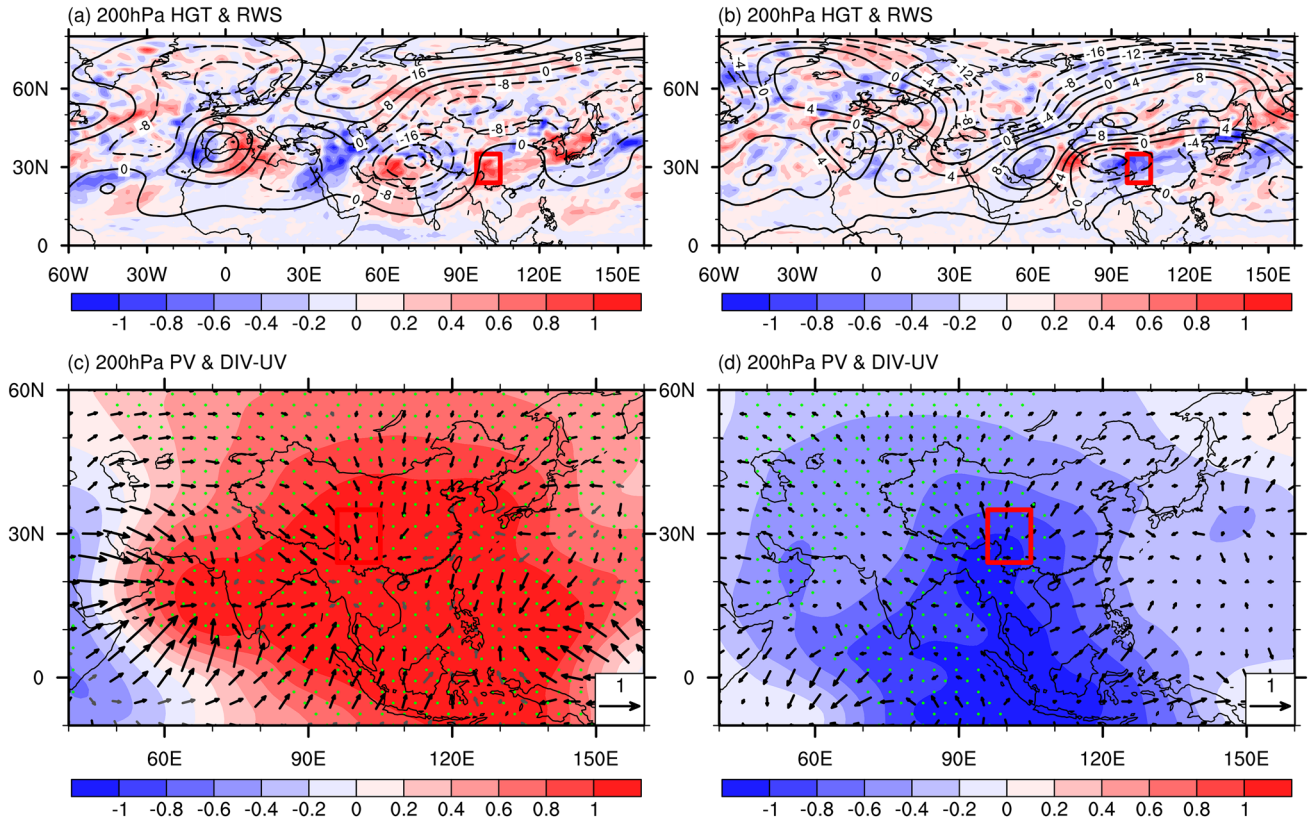

Fig. 13 Regression of 200 hPa geopotential height (contour; gpm) in May and October with respect to the normalized **a** onset and **b** cessation dates over the HM, respectively, and 200 hPa Rossby wave sources (shaded; 10^{-10} s^{-2}) based on the regressed 200 hPa wind anomalies. Regression of 200 hPa potential velocity (shaded; 10^6 m^2 s^{-1}) and 200 hPa divergent winds (vector; m s^{-1}) in May and October with respect to the normalized **c** onset and **d** cessation dates over the HM, respectively. Green dots and black bold vectors indicate that the confidence level reaches 90%

(Fig. 12a, b). Ding and Wang (2005) mentioned that the atmospheric circulation anomalies near India play the active role in undertaking the upstream and downstream wave train of SRP. Meanwhiles, the Rossby wave sources have been demonstrated to be important to inducing the SRP (Enomoto et al. 2003; Kosaka et al. 2009; Chen and Huang 2012; Hong et al. 2018). Thus, Fig. 13a, b present the 200 hPa linearized barotropic Rossby wave sources for onset and cessation dates, respectively, and the linearized barotropic Rossby wave source S can be written as (Sardeshmukh and Hoskins 1988):

$$S = -\nabla \cdot \left[\mathbf{V}_{\chi}^{'}\left(f + \overline{\zeta}\right)\right] - \nabla \cdot \left(\overline{\mathbf{V}}_{\chi}\zeta^{'}\right), \tag{6}$$

where $\mathbf{V}_{\chi} = \left(u_{\chi}, v_{\chi}\right)$ is the horizontal divergent wind components, and the other symbols are consistent with the definition in the previous sections. Positive and negative Rossby wave sources appear alternatively along the jet stream both for interannual variation of onset and cessation dates (Figs. 12a, b, 13a, b). In particular, the strong negative (positive) geopotential height anomalies on the north side of the AS coincide the nearby positive (negative) Rossby wave source for onset (cessation) dates, and the planetary vorticity stretching term ($-f\nabla \cdot \mathbf{V}_{\chi}^{'}$) plays the dominant role in generating Rossby wave source there (figure not shown). For onset dates, the positive SST and wet anomalies over the southwest IO induce the upper-level convergence wind and convergence anomalies near the AS, reinforcing the north side negative geopotential height anomalies via the positive Rossby wave source due to the role of $-f\nabla \cdot \mathbf{V}_{\chi}^{'}$ (Figs. 11a, c, 13a, c). Similarly, for cessation dates, the negative SST and precipitation anomalies over the equatorial west IO cause the upper-level divergence wind and divergence anomalies near the AS, thus that the resultant negative $-f\nabla \cdot \mathbf{V}_{\chi}^{'}$ and Rossby wave source further enhances the positive geopotential height anomalies on the north side of the AS (Figs. 11b, d, 13b, d).

6 Summary

In this study, the onset and cessation of rainy season over the HM are determined by an objective method for the first time. Besides, the climatological and interannual characteristics of onset and cessation dates, as well as the involved physical processes and the possible influencing factors, are investigated based on multiple observational and reanalysis datasets. The obtained results improve the understanding of the rainy season over the HM, and contribute to the research on the regional monsoon climate. For all stations over the HM, the climatological onset dates show clear geographically inhomogeneous, while the differences of climatological cessation dates among the stations are relatively small. Thus, the length of climatological rainy season depends largely on the climatological onset date. The climatological total precipitation exhibits a decreasing tendency from the southern to northern HM, indicating the more crucial role of the precipitation rate rather than length of rainy season. The climatological rainy season for the HM starts at 13 May and ends at 5 October, and its length is 151 days, consistent with the previous definition of the rainy season from May to September over the HM based on the climatological monthly precipitation (Gao et al. 2013; Dong et al. 2018, 2019; Tao et al. 2020).

The onset of climatological rainy season in the HM is triggered by the strengthened lower-level southerlies at the southwest side of HM, accompanying by the moisture convergence and upward motions over the HM. The southerlies are strengthened due to the enhanced southwesterlies the AS, denoting the onset of ISM. The upper-level circulation shows the northward shift of 200 hPa subtropical jet and establishment of South Asian high. Instead, the cessation of climatological rainy season in the HM is related to the withdrawal of ISM, and the resultant lower-level northerly anomalies at the southwest side of HM lead to the moisture divergence and downward motions over the HM. Moreover, the 200 hPa subtropical jet shifts southward, and the South Asian high weakens and withdraws.

Both onset and cessation dates exhibit strong interannual variability with the standard deviation of 12 and 10 days, respectively. Corresponding to the late onset, the northeasterly wind anomalies at lower levels extend from the north IO to HM, and delay the advance of moisture transported by ISM. In addition, the northeasterly wind anomalies cooperate with the westerly wind anomalies at the north flank of the anomalous NWP anticyclone and the HM local topography, leading to the anomalous moisture divergence and downward motions. Besides, a dipole pattern of anomalous circulation at upper levels appears around the HM. The negative geopotential height anomalies with a closed cyclonic circulation are coupled with the negative temperature anomalies on the north side of the AS. The climatological zonal winds advect the anomalous cold air to the HM, and the northwesterly anomalies advect climatological relative cold air from high latitudes to the southeast corner of HM. The late onset related downward motion anomalies over the HM are mainly affected by these two cold advection processes represented by the terms of $\overline{u}\frac{\partial T'}{\partial x}$ and $v'\frac{\partial \overline{T}}{\partial y}$ in omega equation.

The lower-level northeasterly anomalies over the north IO are part of C-shaped wind anomalies, which are excited by the positive SST anomalies over the southwest IO as a result of the Coriolis force (Wu et al. 2008; Du et al. 2009; Wu and Yeh 2010). The anomalous anticyclone over the NWP is triggered as a Rossby wave response to the local cooling and by the remote teleconnection of the El Niño-like CEP warming (Wang et al. 2000; Wu et al. 2017; Tao et al. 2019). At upper levels, two wave trains are observed over Eurasia, and the whole structure highly resembles the SRP (Lu et al. 2002; Enomoto et al. 2003; Kosaka et al. 2009). Especially, the closed anomaly center of 200 hPa geopotential height on the north side of the AS is stronger than other centers, and coincide the nearby positive Rossby wave source. The positive SST anomalies over the southwest IO induce the upper-level convergence wind and convergence anomalies near the AS, reinforcing the north side negative geopotential height anomalies via the positive Rossby wave source due to the role of $-f\nabla\cdot\mathbf{V}'_{\chi}$. Figure 14a shows the schematic diagram illustrating that the combined effects of atmospheric wave train and SST influence the onset of rainy season over the HM.

In accord with late cessation, the cyclonic wind anomalies over the north IO and the anticyclonic wind anomalies over the NWP merge into the anomalous southerlies on the south side of HM, causing the anomalous moisture convergence and upward motions over the HM. An upper-level dipole pattern appears over the Iran and TP, shifting more westward and in opposite spatial distribution compared with the results related to the onset dates. Analysis of the omega equation reveals that $v'\frac{\partial \overline{T}}{\partial y}$ and $\overline{u}\frac{\partial \zeta'}{\partial x}$ jointly contribute to anomalous upward motions over the HM. $v'\frac{\partial \overline{T}}{\partial y}$ related positive temperature advection corresponds well with the ascending anomalies around the HM, and the anomalous southwesterly anomalies advect climatological warm air form the tropics to the HM. The dipole pattern of anomalous circulation cooperating with the climatological zonal westerlies leads to the dipole structure of vorticity advection at upper levels. The positive vorticity advection around the HM decreases with increasing pressure level, and the resulting negative vertical difference of vorticity advection peaks at around 400 hPa and coincides with the ascending anomalies.

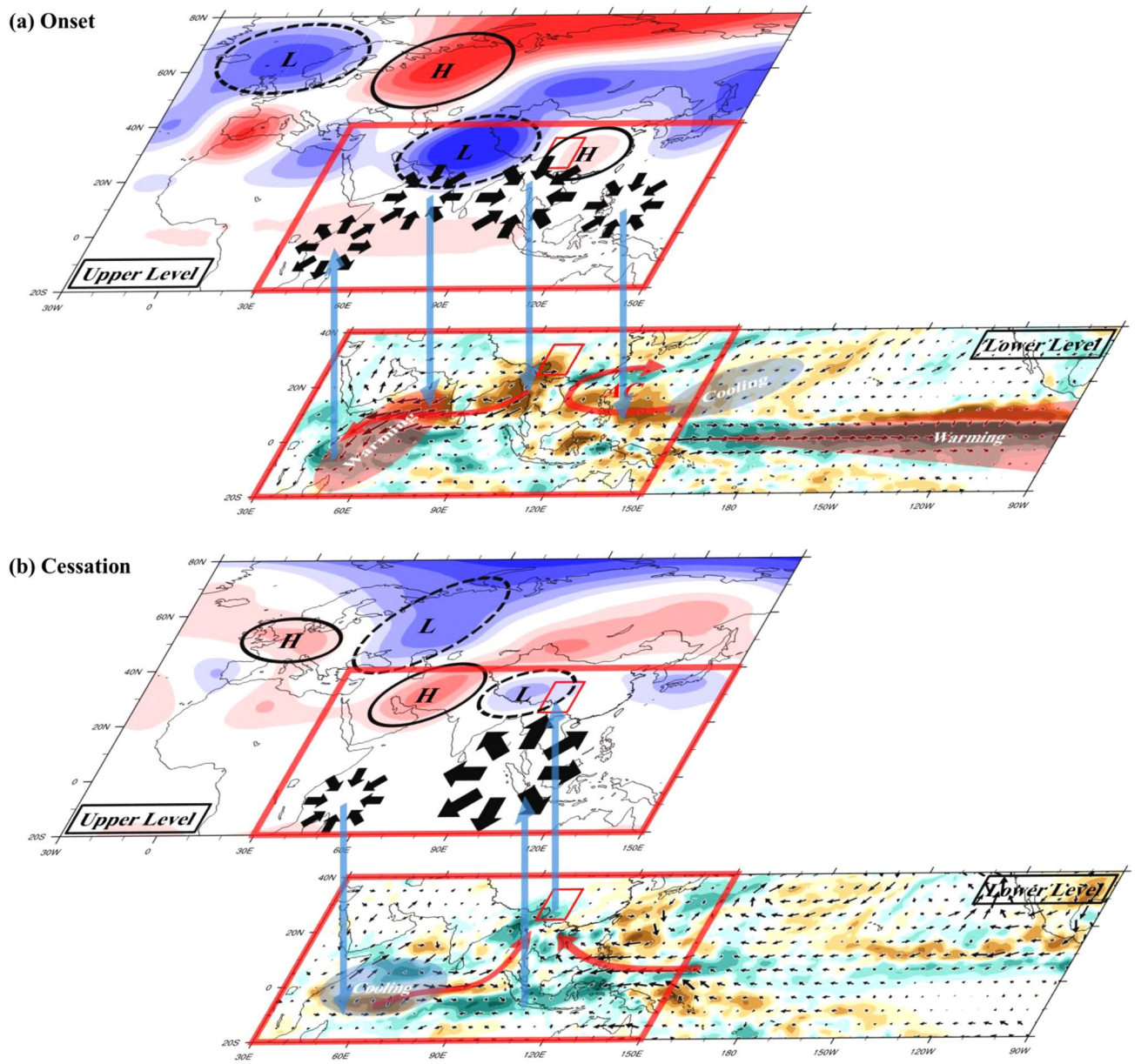

Fig. 14 Schematic diagrams illustrate the combined effects of atmospheric wave train and SST affecting the **a** onset and **b** cessation of rainy season over the HM. Bottom panels in **a** and **b** are the regression of 850 hPa winds (vector, m s^{-1}) and precipitation (shaded, mm) in May and October with respect to the normalized onset and cessation dates over the HM, respectively. Top panels in **a** and **b** are the regression of 200 hPa geopotential height (shaded; gpm) in May and October with respect to the normalized onset and cessation dates over the HM, respectively. Red and blue shadings represent positive and negative SST anomalies, respectively. Black arrows represent the upper-level convergence and divergence anomalies. The "H" and "L" in black circles represent anomalous high and low pressure at upper levels, respectively. Red arrows represent lower-level wind anomalies. The "AC" marks the location of the anomalous lower-level anticyclone. Blue arrows represent the anomalous vertical motions

In response to the equatorial west IO cooling, the zonal circulation is adjusted with lower-level westerly and upper-level easterly anomalies over the equatorial IO, causing the anomalous positive precipitation from the equatorial east IO to Maritime Continent. Furthermore, the cyclonic wind anomalies over the northeast IO and easterly anomalies over the western Pacific are triggered as the Rossby and Kelvin wave response to the positive precipitation anomalies respectively, and the two flow channels are merged and turn into southerly anomalies on the south side of HM. The 200 hPa geopotential height anomalies and wave activity fluxes over Eurasia also resemble SRP, and the anomaly center on the north side of the AS is strongest. The negative SST anomalies over the equatorial west IO cause the

upper-level divergence wind and divergence anomalies near the AS, thus that the resultant negative $-f\nabla\cdot\mathbf{V}_{\chi}'$ and Rossby wave source enhances the positive geopotential height anomalies on the north side of the AS. The combined effects of atmospheric wave train and SST affect the cessation of rainy season over the HM are summarized as the schematic diagram in Fig. 14b.

Acknowledgements This work was supported by the Second Tibetan Plateau Scientific Expedition and Research (STEP) program (2019QZKK0102), the Strategic Priority Research Program of Chinese Academy of Sciences (XDA20060501), the National Natural Science Foundation of China (42005132, 42175049, 42141019, 41831175, 91937302, and 41721004). The NCC/CMA observed daily precipitation data can be accessed from http://data.cma.cn/en. The ETOPO1 topography data is available at https://www.ngdc.noaa.gov/mgg/global/global.html. The JRA-55 reanalysis dataset can be accessed from https://jra.kishou.go.jp/. The ERSST dataset is obtained from https://psl.noaa.gov/data/gridded/data.noaa.ersst.v5.html. The GPCP precipitation dataset is provided at https://psl.noaa.gov/data/gridded/data.gpcp.html.

Author contributions WT and GH designed the study. WT collected the data and performed the analysis. GH contributed to improving the analysis and interpretation. PW and YW provided part of the methods. HG and DD prepared part of the data. WT wrote the initial manuscript. All authors discussed and revised the manuscript.

Funding This work was supported by the Second Tibetan Plateau Scientific Expedition and Research (STEP) program (2019QZKK0102), the Strategic Priority Research Program of Chinese Academy of Sciences (XDA20060501), the National Natural Science Foundation of China (42005132, 42175049, 42141019, 41831175, 91937302, and 41721004).

Availability of data and material The NCC/CMA observed daily precipitation data can be accessed from http://data.cma.cn/en. The ETOPO1 topography data is available at https://www.ngdc.noaa.gov/mgg/global/global.html. The JRA-55 reanalysis datasets can be accessed from https://jra.kishou.go.jp/. The ERSST dataset is obtained from https://psl.noaa.gov/data/gridded/data.noaa.ersst.v5.html. The GPCP precipitation dataset is provided at https://psl.noaa.gov/data/gridded/data.gpcp.html. The datasets generated and/or analyzed during the current study are available upon reasonable request from the authors.

Declarations

Conflict of interest The authors declare that they have no conflict of interest.

References

Adler RF, Huffman GJ, Chang A, Ferraro R, Xie P-P, Janowiak J, Rudolf B, Schneider U, Curtis S, Bolvin D, Gruber A, Susskind J, Arkin P, Nelkin E (2003) The version-2 Global Precipitation Climatology Project (GPCP) monthly precipitation analysis (1979–present). J Hydrometeorol 4(6):1147–1167. https://doi.org/10.1175/1525-7541(2003)004%3c1147:tvgpcp%3e2.0.co;2

Agee JK, Wright CS, Williamson N, Huff MH (2002) Foliar moisture content of Pacific Northwest vegetation and its relation to wildland fire behavior. For Ecol Manag 167(1):57–66. https://doi.org/10.1016/S0378-1127(01)00690-9

Amante C, Eakins BW (2009) ETOPO1 1 Arc-Minute Global Relief Model: procedures, data sources and analysis. NOAA Technical Memorandum NESDIS NGDC-24 National Geophysical Data Center: NOAA. https://doi.org/10.7289/V5D798BF

Chen G, Huang R (2012) Excitation mechanisms of the teleconnection patterns affecting the July precipitation in Northwest China. J Clim 25(22):7834–7851. https://doi.org/10.1175/jcli-d-11-00684.1

Cheng Z, Weng C, Guo J, Dai L, Zhou Z (2018) Vegetation responses to late quaternary climate change in a biodiversity hotspot, the Three Parallel Rivers region in southwestern China. Palaeogeogr Palaeoclimatol Palaeoecol 491:10–20. https://doi.org/10.1016/j.palaeo.2017.11.032

Chuvieco E, González I, Verdú F, Aguado I, Yebra M (2009) Prediction of fire occurrence from live fuel moisture content measurements in a Mediterranean ecosystem. Int J Wildland Fire 18(4):430–441. https://doi.org/10.1071/WF08020

Ding T, Gao H (2020) The record-breaking extreme drought in Yunnan Province, Southwest China during Spring-Early Summer of 2019 and possible causes. J Meteorol Res 34(5):997–1012. https://doi.org/10.1007/s13351-020-0032-8

Ding Q, Wang B (2005) Circumglobal teleconnection in the Northern Hemisphere Summer*. J Clim 18(17):3483–3505. https://doi.org/10.1175/jcli3473.1

Dong X, Duan X (1998) Climatic characteristics and variation tendency of precipitation in the southwest region of China (in Chinese). Scientia Meteorologica Sinica 18(3):239–247

Dong W, Lin Y, Wright JS, Ming Y, Xie Y, Wang B, Luo Y, Huang W, Huang J, Wang L, Tian L, Peng Y, Xu F (2016) Summer rainfall over the southwestern Tibetan Plateau controlled by deep convection over the Indian subcontinent. Nat Commun 7:10925. https://doi.org/10.1038/ncomms10925

Dong D, Huang G, Tao W, Wu R, Hu K, Li C (2018) Interannual variation of precipitation over the Hengduan Mountains during rainy season. Int J Climatol 38(4):2112–2125. https://doi.org/10.1002/joc.5321

Dong D, Tao W, Lau WKM, Li Z, Huang G, Wang P (2019) Interdecadal variation of precipitation over the Hengduan Mountains during rainy seasons. J Clim 32(12):3743–3760. https://doi.org/10.1175/jcli-d-18-0670.1

Du Y, Xie SP, Huang G, Hu K (2009) Role of air–sea interaction in the long persistence of El Niño-induced North Indian Ocean warming. J Clim 22(8):2023–2038

Dunning CM, Black ECL, Allan RP (2016) The onset and cessation of seasonal rainfall over Africa. J Geophys Res Atmos 121(19):11405–411424. https://doi.org/10.1002/2016JD025428

Enomoto T, Hoskins BJ, Matsuda Y (2003) The formation mechanism of the Bonin high in August. Q J R Meteorol Soc 129(587):157–178. https://doi.org/10.1256/qj.01.211

Feng L, Li T, Yu W (2014) Cause of severe droughts in Southwest China during 1951–2010. Clim Dyn 43(7):2033–2042. https://doi.org/10.1007/s00382-013-2026-z

Gao Y, Wang H, Li S (2013) Influences of the Atlantic Ocean on the summer precipitation of the southeastern Tibetan Plateau. J Geophys Res Atmos 118(9):3534–3544. https://doi.org/10.1002/jgrd.50290

Harada Y, Kamahori H, Kobayashi C, Endo H, Kobayashi S, Ota Y, Onoda H, Onogi K, Miyaoka K, Takahashi K (2016) The JRA-55 reanalysis: representation of atmospheric circulation and climate variability. J Meteorol Soc Jpn Ser II 94(3):269–302. https://doi.org/10.2151/jmsj.2016-015

Hong X, Lu R, Li S (2018) Asymmetric relationship between the meridional displacement of the Asian Westerly Jet and the Silk

Road pattern. Adv Atmos Sci 35(4):389–396. https://doi.org/10.1007/s00376-017-6320-2
https://www.nature.com/articles/ncomms10925#supplementary-information
Hu K, Xie S-P, Huang G (2017) Orographically anchored El Niño effect on summer rainfall in Central China. J Clim 30(24):10037–10045. https://doi.org/10.1175/jcli-d-17-0312.1
Kobayashi S, Ota Y, Harada Y, Ebita A, Moriya M, Onoda H, Onogi K, Kamahori H, Kobayashi C, Endo H, Miyaoka K, Takahashi K (2015) The JRA-55 reanalysis: general specifications and basic characteristics. J Meteorol Soc Jpn Ser II 93(1):5–48. https://doi.org/10.2151/jmsj.2015-001
Kosaka Y, Nakamura H (2010) Mechanisms of meridional teleconnection observed between a summer monsoon system and a subtropical anticyclone. Part I: the Pacific-Japan pattern. J Clim 23(19):5085–5108. https://doi.org/10.1175/2010jcli3413.1
Kosaka Y, Nakamura H, Watanabe M, Kimoto M (2009) Analysis on the dynamics of a wave-like teleconnection pattern along the summertime Asian jet based on a reanalysis dataset and climate model simulations. J Meteorol Soc Jpn Ser II 87(3):561–580. https://doi.org/10.2151/jmsj.87.561
Li X, Sun J (2020) Rainy season onset over Northeast China and the related atmospheric circulations. Int J Climatol 40(11):4750–4762. https://doi.org/10.1002/joc.6486
Li Y, Xu H, Liu D (2011) Features of the extremely severe drought in the east of Southwest China and anomalies of atmospheric circulation in summer 2006. Acta Meteorol Sin 25(2):176–187. https://doi.org/10.1007/s13351-011-0025-8
Liebmann B, Marengo J (2001) Interannual variability of the rainy season and rainfall in the Brazilian Amazon Basin. J Clim 14(22):4308–4318. https://doi.org/10.1175/1520-0442(2001)014%3c4308:Ivotrs%3e2.0.Co;2
Liebmann B, Bladé I, Bond NA, Gochis D, Allured D, Bates GT (2008) Characteristics of North American summertime rainfall with emphasis on the monsoon. J Clim 21(6):1277–1294. https://doi.org/10.1175/2007jcli1762.1
Liebmann B, Bladé I, Kiladis GN, Carvalho LMV, Senay GB, Allured D, Leroux S, Funk C (2012) Seasonality of African Precipitation from 1996 to 2009. J Clim 25(12):4304–4322. https://doi.org/10.1175/jcli-d-11-00157.1
Lu R-Y, Oh J-H, Kim B-J (2002) A teleconnection pattern in upper-level meridional wind over the North African and Eurasian continent in summer. Tellus A 54(1):44–55. https://doi.org/10.1034/j.1600-0870.2002.00248.x
Luo K, Quan X, He B, Yebra M (2019) Effects of live fuel moisture content on wildfire occurrence in fire-prone regions over Southwest China. Forests 10(10):887
Myers N, Mittermeier RA, Mittermeier CG, da Fonseca GAB, Kent J (2000) Biodiversity hotspots for conservation priorities. Nature 403(6772):853–858. https://doi.org/10.1038/35002501
Nie ZL, Gu ZJ, Sun H (2002) Cytological study of Tibetia (Fabaceae) in the Hengduan Mountains region. China J Plant Res 115(1):0017–0022. https://doi.org/10.1007/s102650200003
Sardeshmukh PD, Hoskins BJ (1988) The generation of global rotational flow by steady idealized tropical divergence. J Atmos Sci 45(7):1228–1251. https://doi.org/10.1175/1520-0469(1988)045%3c1228:Tgogrf%3e2.0.Co;2
Simmonds I, Bi D, Hope P (1999) Atmospheric water vapor flux and its association with rainfall over China in summer. J Clim 12(5):1353–1367. https://doi.org/10.1175/1520-0442(1999)012%3c1353:awvfai%3e2.0.co;2
Smith TM, Reynolds RW (2003) Extended reconstruction of global sea surface temperatures based on COADS data (1854–1997). J Clim 16(10):1495–1510. https://doi.org/10.1175/1520-0442-16.10.1495
Tan L, Cai Y, Cheng H, Edwards LR, Lan J, Zhang H, Li D, Ma L, Zhao P, Gao Y (2018) High resolution monsoon precipitation changes on southeastern Tibetan Plateau over the past 2300 years. Quatern Sci Rev 195:122–132. https://doi.org/10.1016/j.quascirev.2018.07.021
Tao W, Huang G, Wang P, Liu Y, Wen G, Dong D (2019) Dominant modes of CMIP3/5 models simulating northwest Pacific circulation anomalies during post-ENSO summer and their SST dependence. Theor Appl Climatol 138(3):1809–1820. https://doi.org/10.1007/s00704-019-02936-3
Tao W, Huang G, Lau WKM, Dong D, Wang P, Wen G (2020) How can CMIP5 AGCMs' resolution influence precipitation in mountain areas: the Hengduan Mountains? Clim Dyn 54(1):159–172. https://doi.org/10.1007/s00382-019-04993-w
Tao W, Huang G, Dong D, Wang P, Yu T, Gong H (2021) Dominant modes of interannual variability in precipitation over the Hengduan Mountains during rainy seasons. Int J Climatol 41(4):2795–2809. https://doi.org/10.1002/joc.6990
Tian X-r, Zhao F-j, Shu L-f, Wang M-y (2010) Hotspots from satellite monitoring and forest fire weather index analysis for Southwest China. For Res 4(23):523–529
Tian X-r, Zhao F-j, Shu L-f, Wang M-y (2014) Changes in forest fire danger for south-western China in the 21st century. Int J Wildland Fire 23(2):185–195. https://doi.org/10.1071/WF13014
Wang B, Wu RG, Fu XH (2000) Pacific-East Asian teleconnection: how does ENSO affect East Asian climate? J Clim 13(9):1517–1536. https://doi.org/10.1175/1520-0442(2000)013%3c1517:peathd%3e2.0.co;2
Wang B, Wu R, Lau KM (2001) Interannual variability of the Asian Summer Monsoon: contrasts between the Indian and the Western North Pacific-East Asian Monsoons*. J Clim 14(20):4073–4090. https://doi.org/10.1175/1520-0442(2001)014%3c4073:ivotas%3e2.0.co;2
Wang Z, Ren F, Sun L, Liu Y, Wang P, Tang J, Wang D, Li D (2012) Analysis of climate anomaly and causation in summer 2011 (in Chinese). Meteorol Mon 4:448–455
Wang L, Chen W, Zhou W, Huang G (2015) Drought in Southwest China: a review. Atmos Ocean Sci Lett 8(6):339–344. https://doi.org/10.3878/AOSL20150043
Wang L, Chen W, Zhou W, Huang G (2016) Understanding and detecting super-extreme droughts in Southwest China through an integrated approach and index. Q J R Meteorol Soc 142(694):529–535. https://doi.org/10.1002/qj.2593
Wang T, Zhao Y, Xu C, Ciais P, Liu D, Yang H, Piao S, Yao T (2021) Atmospheric dynamic constraints on Tibetan Plateau freshwater under Paris climate targets. Nat Clim Change. https://doi.org/10.1038/s41558-020-00974-8
Wei W, Zhang R, Wen M, Rong X, Li T (2014) Impact of Indian summer monsoon on the South Asian high and its influence on summer rainfall over China. Clim Dyn 43(5):1257–1269. https://doi.org/10.1007/s00382-013-1938-y
Wu R, Yeh S-W (2010) A further study of the tropical Indian Ocean asymmetric mode in boreal spring. J Geophys Res Atmos 115(D8):D08101. https://doi.org/10.1029/2009jd012999
Wu R, Kirtman BP, Krishnamurthy V (2008) An asymmetric mode of tropical Indian Ocean rainfall variability in boreal spring. J Geophys Res Atmos 113(D5):D05104. https://doi.org/10.1029/2007jd009316
Wu B, Zhou T, Li T (2017) Atmospheric dynamic and thermodynamic processes driving the Western North Pacific anomalous anticyclone during El Niño. Part I: maintenance mechanisms. J Clim 30(23):9621–9635. https://doi.org/10.1175/jcli-d-16-0489.1
Xing Y, Ree RH (2017) Uplift-driven diversification in the Hengduan Mountains, a temperate biodiversity hotspot. Proc Natl Acad Sci 114(17):E3444–E3451. https://doi.org/10.1073/pnas.1616063114

Zhang W, Jin F-F, Zhao J-X, Qi L, Ren H-L (2013) The possible influence of a nonconventional El Niño on the severe autumn drought of 2009 in Southwest China. J Clim 26(21):8392–8405. https://doi.org/10.1175/jcli-d-12-00851.1

Zhang P, Li G, Fu X, Liu Y, Li L (2014) Clustering of Tibetan Plateau vortices by 10–30-day intraseasonal oscillation. Mon Weather Rev 142(1):290–300. https://doi.org/10.1175/mwr-d-13-00137.1

Zhang T, Li B, He Y, Du J, Niu H, Xin H (2015) Spatial and temporal distribution of precipitation based on corrected TRMM data in Hengduan Mountains (in Chinese). J Nat Resour 30(2):260–270

Zhao G, Huang G, Wu R, Tao W, Gong H, Qu X, Hu K (2015) A new upper-level circulation index for the East Asian summer monsoon variability. J Clim 28(24):9977–9996. https://doi.org/10.1175/JCLI-D-15-0272.1

Zhou C, Jiang X, Li Y, Wei G (2009) Features of climate change of water vapor resource over Eastern region of the Tibetan Plateau and its surroundings (in Chinese). Plateau Meteorol 28(1):55–63

Zhu G, Pu T, Zhang T, Liu H, Zhang X, Liang F (2013) The accuracy of TRMM precipitation data in Hengduan Mountainous Region, China (in Chinese). Scientia Geographica Sinica 33(9):1125–1131. https://doi.org/10.13249/j.cnki.sgs

Zhu G, Qin D, Tong H, Liu Y, Li J, Chen D, Wang K, Hu P (2016) Variation of Thornthwaite moisture index in Hengduan Mountains, China. Chin Geogr Sci 26(5):687–702. https://doi.org/10.1007/s11769-016-0820-3